

Carrier-induced antiferromagnet of graphene islands embedded in hexagonal boron nitride

Ashwin Ramasubramaniam

Department of Mechanical and Industrial Engineering, University of Massachusetts, Amherst, Massachusetts 01003, USA

Doron Naveh

Department of Electrical and Computer Engineering, Carnegie Mellon University, Pittsburgh, Pennsylvania 15213, USA

(Received 31 March 2011; revised manuscript received 10 May 2011; published 1 August 2011)

Graphene islands with zigzag edges embedded in nitrogen-terminated vacancies in hexagonal boron nitride are shown to develop intrinsic magnetism and preferentially order antiferromagnetically. The magnetic moment of each graphene island is given by the numerical imbalance of carbon atoms on its two sublattices, which is in turn directly related to the size of the host defect. We propose a carrier-mediated model for antiferromagnetic coupling between islands and estimate Néel temperatures for these structures in excess of 100 K in some instances, with the possibility of attaining even higher temperatures at higher island densities. Our results suggest the possibility of designing molecular magnets via defect engineering of hexagonal boron nitride templates followed by trapping of carbon atoms in the defects.

DOI: [10.1103/PhysRevB.84.075405](https://doi.org/10.1103/PhysRevB.84.075405)

PACS number(s): 73.22.Pr

I. INTRODUCTION

Magnetism in materials that contain only s and p electrons is of fundamental and technological interest, with potential applications in spintronic devices and molecular magnets for quantum computing.¹ Carbon is an intriguing candidate in this aspect, in light of several reports of magnetism in its nanoscale allotropes (fullerenes, nanotubes, graphene).² The recent spate of research on graphene has generated several reports of intrinsic magnetism in graphene nanodots,³ zigzag nanoribbons,⁴ defective sheets (with vacancies, holes, cracks),⁵ and antidot lattices.⁶ Similarly, extrinsic factors such as substrates,⁷ adsorbates (H, C, N),⁸ group I-III metals,⁹ and dopants¹⁰ are also reported to induce magnetism in graphene. In general, the disruption of graphene π bonds by intrinsic or extrinsic factors leads to a finite density of states near the Fermi level; exchange interactions induce spin splitting, which in turn leads to itinerant magnetism.

Hexagonal boron nitride (hBN)—an insulating isoelectronic, isomorph of graphene—has captured recent interest as a superior dielectric substrate for graphene electronics.¹¹ Intriguingly, the synthesis of coexisting domains of hBN and graphene within a single sheet has also been demonstrated experimentally;¹² analogous structures have been known for some time now in the context of heteronanotubes.¹³ Such graphene-hBN hybrids, which have properties different from either of their constituents, could open up entirely new possibilities in electronic, optical, and nanomechanical applications. Previous density functional theory (DFT) studies have shown that a substitutional C atom in an hBN nanotube¹⁴ or sheet¹⁵ possesses a net magnetic moment of $1 \mu_B$ independent of substitutional site (B or N); this state is associated with a defect level within the (wide) hBN band gap. DFT studies have also shown the existence of half-metallicity in hybrid BNC nanoribbons¹⁶ and nanotubes.¹⁷ Other DFT studies have investigated the size and stoichiometry dependence of the electronic structure of graphene islands embedded in hBN layers.¹⁸ In this paper, we investigate the magnetic interactions of graphene *islands*, rather than individual C atoms, embedded in hBN.

In this work, we consider a hexagonal array of graphene islands embedded in an infinite hBN sheet (Fig. 1). This configuration does not suffer from geometric frustration and allows for both ferro- (FM) and antiferromagnetic (AFM) nearest-neighbor coupling of islands. Each island is a *triangular* C_4 substitutional cluster in a B_3N vacancy site. This island structure is motivated by high-resolution TEM experiments,¹⁹ which clearly document such triangular N-terminated vacancies (B_3N and larger) as a consequence of electron-beam damage; we envision such vacancies acting as “host-defects” for C islands. We focus on the magnetic interactions between these C_4 clusters, as a function of spacing, with the goal of identifying the magnetic ground state and extracting exchange coupling coefficients.

The remainder of this paper is organized as follows. Details of DFT calculations are provided in Sec. II. Section III provides results of electronic structure calculations on C_4 islands embedded in hBN with estimates for Néel temperatures as a function of island spacing. We also elucidate the underlying physical mechanisms behind exchange coupling between islands in Sec. III. Concluding remarks are provided in Sec. IV. Additional details on estimating island magnetic moments by direct integration of the spin density are provided in Appendix A. The sensitivity of our predictions to the choice of DFT exchange-correlation functionals is examined in Appendix B.

II. COMPUTATIONAL METHODS

DFT calculations were performed using the Vienna *Ab Initio* Simulation Package.²⁰ Core and valence electrons were described using projector-augmented waves.²¹ Electron exchange and correlation (XC) was treated using the local spin density approximation (LSDA), which is implemented in VASP following the Perdew-Zunger parametrization²² of the Ceperley–Alder data.²³ (Additional tests with different XC functionals are reported in Appendix B.) hBN sheets with 6, 9, 12, and 15 unit cells on edge (72, 162, 288, and 450 atoms, respectively) were constructed at the LSDA lattice parameter

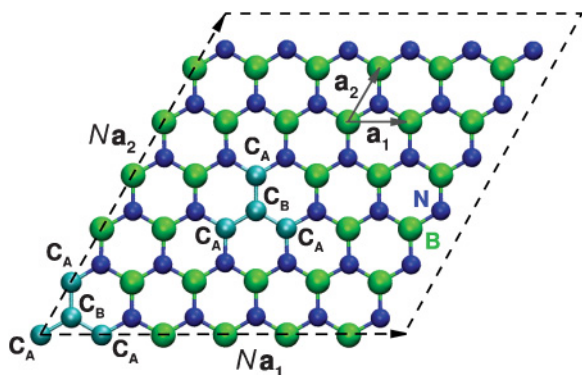


FIG. 1. (Color online) Hexagonal array of graphene islands in an hBN lattice with N primitive cells on edge. The primitive vectors \mathbf{a}_1 and \mathbf{a}_2 of hBN are of length $a_0 = 2.488 \text{ \AA}$. C atoms on the A and B sublattice are indicated by C_A and C_B . The center-to-center distance between islands is $r_{nm} = Na_0/\sqrt{3}$. Dotted lines enclose the periodic simulation cell.

of 2.488 \AA . Selected B and N atoms were replaced with C atoms to form a hexagonal array of islands. Periodic images were separated by 15 \AA of vacuum normal to the sheet to prevent spurious image interactions. Atomic positions were relaxed with a force tolerance of 0.02 eV/\AA in a nonmagnetic calculation. The relaxed nonmagnetic configuration was employed in subsequent spin-polarized, single-point calculations to obtain energies for ferro- and antiferromagnetically coupled configurations. A $2 \times 2 \times 1$, Γ -centered k -point mesh was used for the $N = 6$ supercell whereas a single Γ point was employed for larger cells. The kinetic energy cutoff was set to 400 eV . Electronic minimization was performed with a

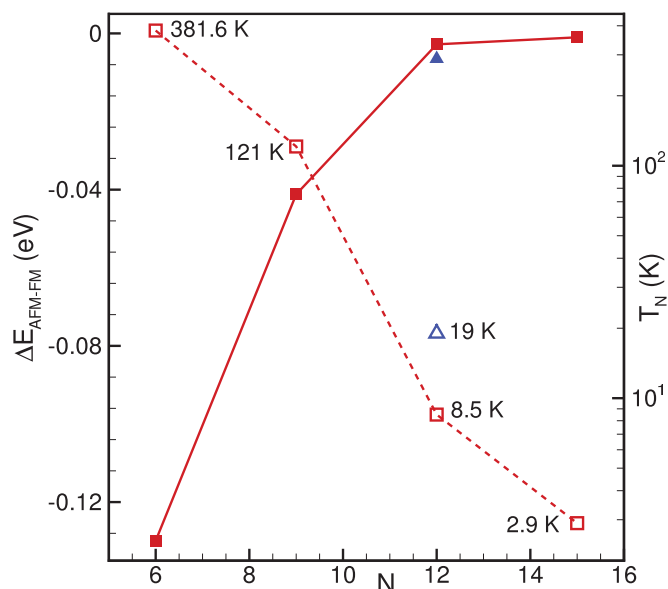


FIG. 2. (Color online) Energy difference between AFM and FM coupled C_4 islands as a function of separation N (solid squares) and Néel temperatures for AFM-coupled C_4 islands (hollow squares). AFM coupling is distinctly favored at small island spacings with correspondingly higher Néel temperatures. The lines are a guide to the eye. Blue triangles are for a C_9 island in an $N = 12$ simulation cell, indicating that increasing the island size while keeping the island spacing constant can serve to tune the Néel temperature of the array.

tolerance of 10^{-4} eV . A Gaussian smearing of 0.05 eV was used in all calculations.

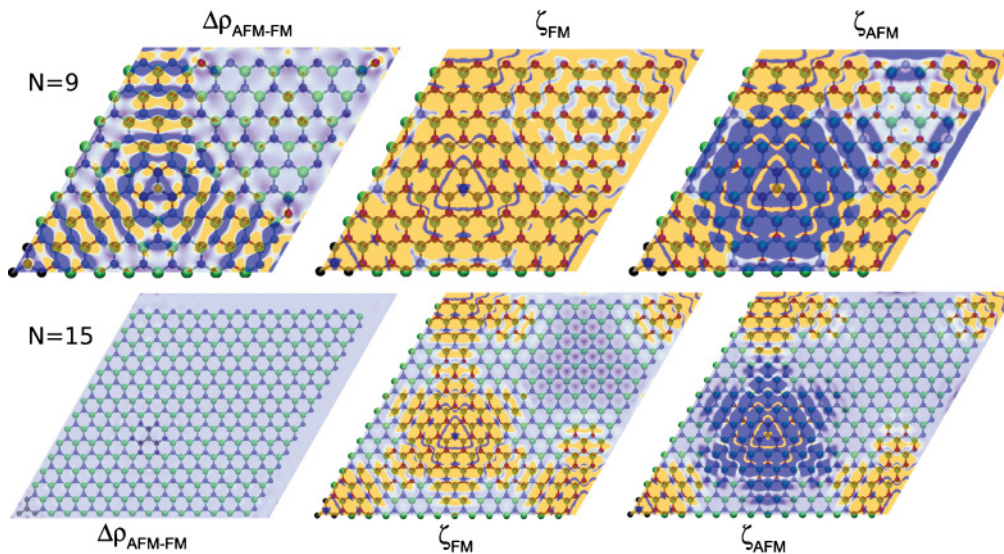


FIG. 3. (Color online) Charge difference $\Delta\rho_{\text{AFM-FM}}$ between AFM and FM coupled C_4 islands and relative spin density $\zeta = (\rho_{\uparrow} - \rho_{\downarrow})/(\rho_{\uparrow} + \rho_{\downarrow})$ for each case projected on the atomic plane for an $N = 9$ cell (upper row) and $N = 15$ cell (lower row). (Light) Yellow and (dark) blue regions correspond to values of $\Delta\rho_{\text{AFM-FM}} \geq 10^{-4} \text{ e/\AA}^2$ and $\leq -10^{-4} \text{ e/\AA}^2$, respectively, as well as $\zeta \geq 10^{-4}$ and $\leq -10^{-4}$, respectively. As seen from the ζ plots, each C_4 island spin-polarizes its BN neighbors due to its two unpaired electrons thereby inducing exchange interactions between islands. The $\Delta\rho$ plots show alternating belts of charge depletion and accumulation that are indicative of varying degrees of charge transfer between the islands and the hBN matrix depending upon the magnetic coupling between islands (FM or AFM). The charge transfer is mediated entirely via the p_z orbitals of C, B, and N. The differences are more obvious for the $N = 9$ case; for $N = 15$ the differences are very small (near-degenerate AFM and FM configurations) and are localized to the immediate vicinity of the islands.

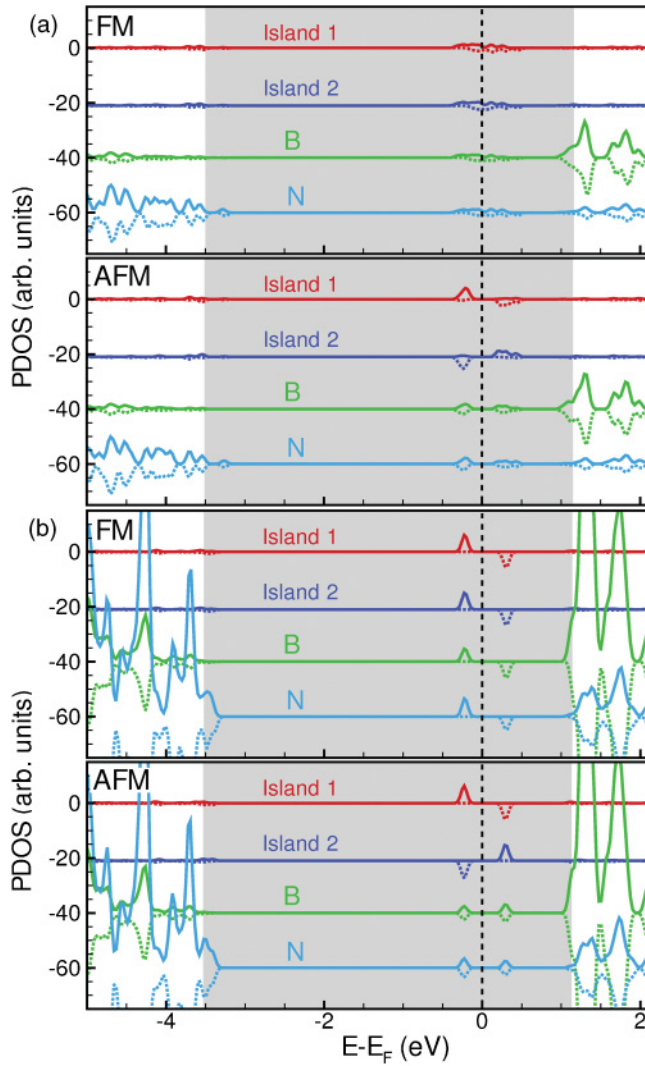


FIG. 4. (Color online) Decomposition of the total density of states of the (a) $N = 6$ and (b) $N = 15$ simulation cells into contributions from each graphene island and the B and N atoms. α and β spin channels are indicated by solid and dotted lines, respectively. (For clarity, the β channel is reflected in the x axis; individual curves are rigidly shifted along the y axis.) The shaded region indicates the LSDA band gap region (~ 4.66 eV) of a pure hBN layer.

III. RESULTS AND DISCUSSION

We consider first the energetics of FM and AFM coupled islands embedded in hBN. Fig. 2 displays the difference in ground-state energies between AFM and FM coupled islands as a function of island spacing. As evident from these data, the AFM state is consistently energetically preferred over the FM state. The energy difference between the FM and AFM states is inversely proportional to the island spacing, ranging from 130 meV for the smallest spacing ($N = 6$, $r_{nn} \approx 8.62$ Å) to 1 meV for the largest spacing ($N = 15$, $r_{nn} \approx 21.55$ Å).

Within each C_4 island, the two graphene sublattices are antiferromagnetically coupled to each other (Fig. 3). As seen from Fig. 1, within each island there is an excess of two C atoms on the A sublattice as compared to the B sublattice; Lieb's theorem²⁴ then suggests a net magnetic moment of

$2 \mu_B$ arising from each island. Indeed, for the FM case, we obtain a *total* magnetic moment of $4 \mu_B$ ($2 \mu_B$ per island) for the $N = 9, 12, 15$ simulation cells. Note that the spins are not entirely localized on the C atoms (Fig. 3), but the decay in spin density away from the island is sufficiently rapid that for $N \gtrsim 15$ the islands are essentially noninteracting. However, when islands are close their interaction is strong enough to partially quench the magnetic moment, specifically to $0.7 \mu_B$ per island for the FM $N = 6$ cell. For all AFM cases, the net magnetic moment for the simulation cell is obviously zero, but magnetic moments per island can be estimated by explicitly integrating the spin density (Appendix A). Proceeding thus, we recover magnetic moments of approximately $\pm 2 \mu_B$ for weakly interacting islands. For the $N = 6$ cell we estimate an average moment of $\pm 1.19 \mu_B$ per island; the departure from the expected value of $\pm 2 \mu_B$ is again indicative of strong island-island interactions, albeit to a lesser degree than in the FM case where the average moment per island is quenched to about $0.7 \mu_B$.

We now examine the electronic structure of this hybrid C-BN sheet in greater detail. Figure 4 displays the density of states decomposed into partial contributions from each C_4 island and from the B and N atoms for the $N = 6$ and 15 cells, respectively. The corresponding band structure plots are displayed in Fig. 5. First, we consider the $N = 15$ case ($N = 9$ and 12 are essentially identical). It is apparent that the spin channels are degenerate below the valence band edge and above the conduction band edge of pristine hBN. The C_4 islands act as impurities, injecting defect levels within the bulk hBN band gap, which undergo spin splitting. Depending upon FM or AFM coupling of islands, we obtain four singly-occupied flat bands from the same spin channel (two bands for two unpaired electrons per island) or two singly-occupied flat bands from each spin channel, respectively [Fig. 5(b)]. The band gap is 1.34 eV and 0.84 eV for FM and AFM cases, respectively. The sole contribution to the flat bands arises from p_z electrons of C, B, and N atoms (Fig. 6). Similar results have been reported previously for single C substitutionals in BN nanotubes and sheets.^{14,15} The $N = 6$ case presents a slightly more complex picture. For the AFM case the defect states are still localized near the Fermi level [Fig. 4(a)], although the associated bands now show some dispersion [Fig. 5(a)]. For the FM case though, there is a *finite* density of states in both spin channels at the Fermi level. Thus, the stable AFM to metastable FM transition is accompanied by a transition from a semiconducting to a metallic state.

To estimate Néel temperatures for the AFM ground states of this C-BN sheet, we employ a simple Ising model with nearest-neighbor exchange. The Hamiltonian for this model is $\mathcal{H} = \sum_{\langle \alpha, \beta \rangle} J_{\alpha\beta}(r_{\alpha\beta}) \sigma_\alpha \sigma_\beta$, where $J_{\alpha\beta}(r_{\alpha\beta})$ is the exchange coupling between nearest neighbors α and β , and σ_α and σ_β are the magnetic moments of each island (normalized to ± 1); the energy difference between the AFM and FM cases is $\Delta E_{\text{AFM-FM}} = -6J_{\alpha\beta}(r_{\alpha\beta})$ (per simulation cell with two islands). Admittedly, this lumping of spatially distributed spins into a single magnetic moment at the vertices of a hexagonal lattice is a gross approximation. However, since the spin-density decays very rapidly with distance from the C_4 islands, we expect this to be a reasonable approximation for well-separated islands ($N = 9, 12, 15$). For the $N = 6$

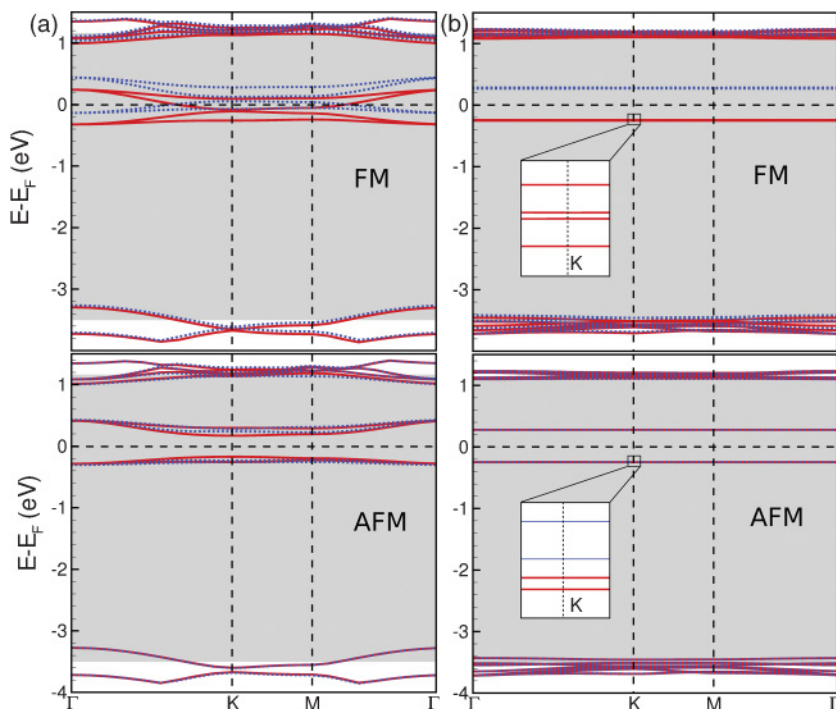


FIG. 5. (Color online) Band structure of FM and AFM coupled islands for the (a) $N = 6$ and (b) $N = 15$ supercells. Solid red (dotted blue) lines denote α (β) spin channels. Only bands in the vicinity of the Fermi level are shown for clarity. For the $N = 6$ supercell, the metastable FM case is *metallic*; the stable AFM case is *semiconducting* with some curvature to the defect levels. For the $N = 15$ supercell, both FM and AFM cases are semiconducting. As shown in the insets in (b), the flat thick lines near the Fermi level are actually composed of four individual dispersionless defect levels which correspond to the peaks seen in Fig. 4 near the Fermi level; these defect levels are near-degenerate and separated by ~ 1 meV. The shaded region indicates the LSDA band gap region (~ 4.66 eV) of a pure hBN layer.

simulation cell, it is clear that strong interactions between islands warrant a more sophisticated treatment.²⁵

Applying the Ising model to the data in Fig. 2 and using the exact solution $T_N = 2J/[k_B \log(2 - \sqrt{3})]$ for the Néel temperature (T_N) of an AFM Ising model on a honeycomb lattice,²⁶ we estimate $T_N = 121$ K, 8.5 K, and 2.9 K for the $N = 9$, 12, and 15 simulation cells, respectively. Even higher Néel temperatures might be feasible for smaller island spacings (larger J); indeed, B_3N host defects do seem to coexist within a few atomic spacings of each other as seen in HRTEM micrographs.¹⁹ If we apply the Ising model to the $N = 6$ case, notwithstanding the previous caveats, we obtain a Néel temperature of 381.6 K. We stress that this result is at best *suggestive* of room-temperature antiferromagnetism, owing to the utter naivety of the model and all the aforementioned complications at these small island spacings.

Our discussion thus far of triangular C_4 islands carries over in near-exact analogy to larger triangular islands. For example, a hexagonal array of C_9 islands embedded in a B_6N_3 vacancy in an $N = 12$ simulation cell has a net magnetic moment of $3\mu_B$ per island. For this case, we estimate a Néel temperature of 19 K, which is about double that of C_4 islands at the same separation. More generally, from simple counting and Lieb's theorem, a triangular C_{m^2} island embedded in a $B_{m(m+1)/2}N_{m(m-1)/2}$ vacancy (with *zigzag edges*) will contribute a net moment of $m\mu_B$ in the dilute limit. Thus, by controlling island size and spacing, it might be possible to control the Néel temperature of the island array. Calculating exchange coefficients for larger islands with DFT—especially for dilute configurations—is computationally prohibitive. Hopefully, less expensive tight-binding calculations planned in the future will allow for a systematic exploration of coupling between larger islands, multiple islands of mixed size, and different or random spatial orderings of islands.

What are the physical mechanisms of magnetic coupling between C islands? There is as yet no general theory for *sp* magnetism²⁷ but first-principles calculations can provide qualitative insight into the relevant mechanisms. Figure 6 shows the density of states decomposed by orbital and spin channel for each C_4 island as well as the B and N atoms. It is readily seen that the defect states near the Fermi level have contributions solely from p_z states. The remaining s , p_x , and p_y states are several eV away from the Fermi level, being involved in strong σ bonds between atoms, and play no role in island-island coupling. Thus, island-island coupling occurs primarily through electron transfer between the half-filled, empty, and filled p_z orbitals of C, B, and N, respectively.

The remaining question to be addressed here is why AFM coupling is energetically favored. The reason is immediately apparent from the relative spin-density plots in Fig. 3, which show wavefronts of spin density emanating from the islands as they polarize their BN neighbors. For the FM case, the wavefronts are of identical spin; therefore, if the islands are sufficiently close (e.g., $N = 9$), Pauli repulsion prevents complete relaxation of the spin density leading to greater confinement and higher kinetic energy. Conversely, in the AFM case, the wavefronts are of opposite spin allowing for more complete relaxation of the spin density. If the islands are well separated (i.e., beyond the characteristic spin-relaxation distance), the FM and AFM cases are essentially degenerate ($N = 15$).

IV. CONCLUDING REMARKS

In summary, we have studied magnetic interactions between ordered arrays of triangular C islands embedded in an hBN sheet and proposed a carrier-induced model for antiferromagnetic coupling of these islands. From our estimates of Néel

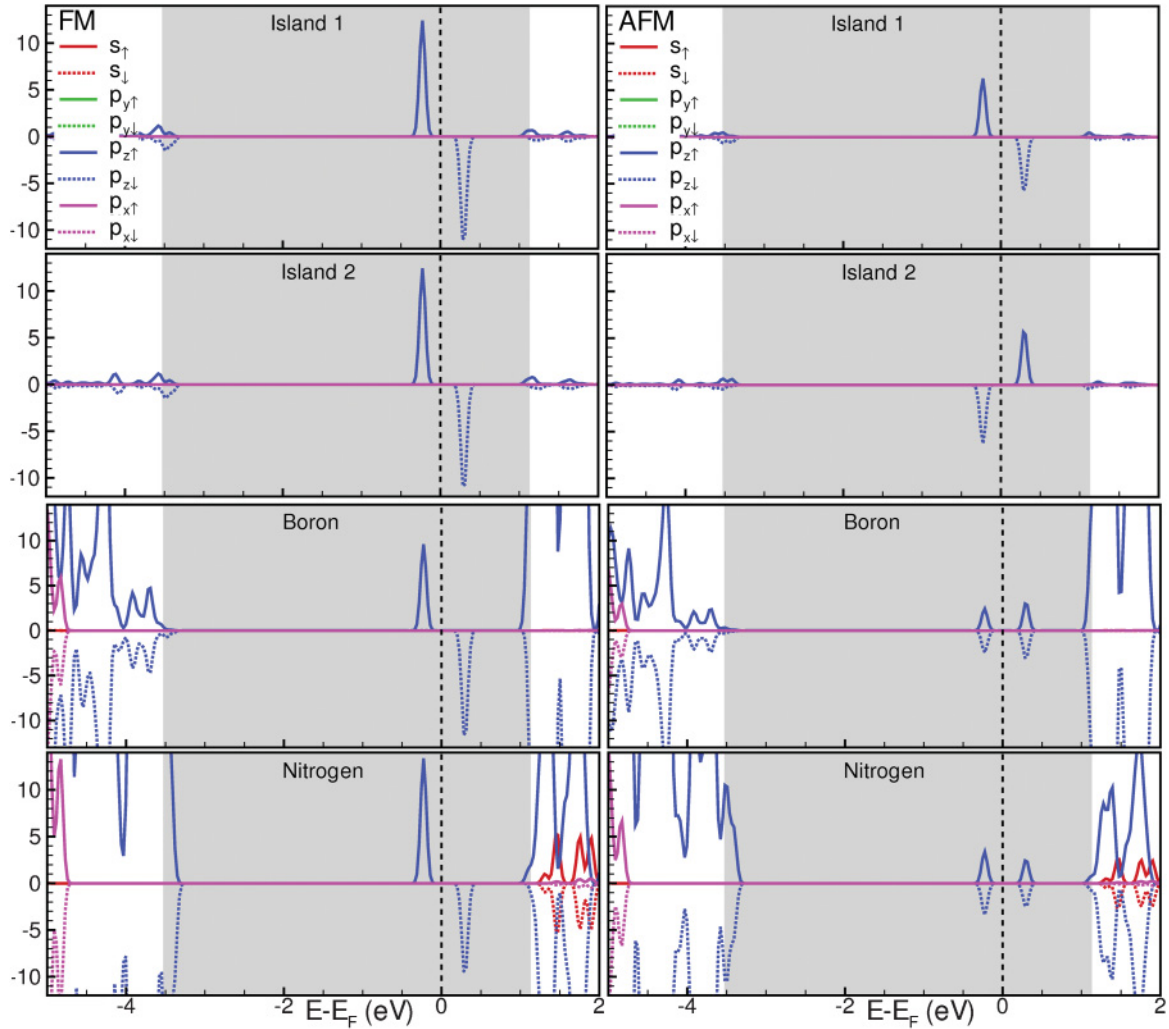


FIG. 6. (Color online) Density of states for the C_4 islands, and the B and N atoms in an $N = 15$ supercell decomposed into contributions from s and p orbitals for each spin channel. As seen, only the p_z orbitals contribute to states near the Fermi level. Therefore island-island coupling occurs primarily through electron transfer between the half-filled, empty, and filled p_z orbitals of C, B, and N, respectively.

temperatures for these arrays, it would appear that attaining room-temperature antiferromagnetism might be possible. The triangular island shapes chosen here were motivated by experiments¹⁹ that clearly show the formation of potential host defects of similar shapes in hBN. We suggest that it might be possible to produce designer molecular magnets by engineering defective hBN templates using electron beam irradiation and trapping C atoms in the defects. We hope our theoretical studies will motivate experiments in this direction.

ACKNOWLEDGMENTS

A.R. gratefully acknowledges research funding from the University of Massachusetts, Amherst.

APPENDIX A: ESTIMATING ISLAND MAGNETIC MOMENTS FROM SPIN DENSITIES

For FM-coupled islands, half the magnetic moment of the supercell can be assigned, on average, to each island. For

the AFM case, the net magnetic moment of the supercell is necessarily zero. To estimate magnetic moments per island, we integrate the spin density over cylinders centered on each island (cylinder axis normal to atomic plane). From symmetry considerations, the radius of the largest cylinder that can be used is half the distance between islands; i.e., $r_{cyl} = r_{nn}/2 = (Na_0)/(2\sqrt{3})$. Table I displays the results for the magnetic moment per island obtained by this integration procedure for the AFM cases. We also list the magnetic moments for the FM cases computed by this procedure to demonstrate the error incurred with respect to the more direct assignment of half the total magnetic moment to each island; as the island separation increases both these values become nearly identical. This is indicative of the spin density being confined to the vicinity of the island. Also note that with the exception of the $N = 6$ case, the integrated density within the cylinder is greater for the FM case as compared to the AFM case. This is a result of greater Pauli repulsion between impinging wavefronts of identical spin polarization emanating from each island in the FM case, leading to greater confinement of spin density.

TABLE I. Magnetic moments per island (in μ_B) for FM and AFM coupled islands in a supercell of size N . M_{int} is the magnetic moment obtained by explicit integration (averaged over both islands); M_{tot} is the total magnetic moment of the supercell. As island separation increases, M_{int} approaches $M_{\text{tot}}/2$.

N	r_{cyl} (Å)	FM		AFM	
		M_{int}	$M_{\text{tot}}/2$	M_{int}	$M_{\text{tot}}/2$
6	4.31	0.56	0.7	± 1.19	0
9	6.46	1.83	2.0	± 1.73	0
12	8.62	1.92	2.0	± 1.91	0
15	10.77	1.96	2.0	± 1.96	0

APPENDIX B: INFLUENCE OF EXCHANGE-CORRELATION FUNCTIONAL ON NÉEL TEMPERATURES

While the results in the text have been obtained using the LSDA to describe exchange and correlation (XC), it is important to recognize that the energy differences (and consequently Néel temperatures) can be sensitive to the choice of functional. While we fully expect that the fundamental physics is unlikely to be grossly altered by the choice of XC functional, we also employ the Perdew-Burke-Ernzerhof (PBE) form²⁸ of the generalized gradient approximation as an additional check on our results. Furthermore, for the $N = 6$ supercell, we additionally employed the Heyd-Scuseria-Ernzerhof (HSE06)²⁹ and PBE0³⁰ hybrid XC functionals, both of which contain a fraction of exact Hartree-Fock exchange and in general provide more accurate band gaps than semilocal XC functionals.³¹ Due to the computational cost of hybrid

TABLE II. Dependence of Néel temperature on XC functional

N	T_N (K)			
	LSDA	PBE	PBE0	HSE06
6	381.6	306.2	131.2	142.8
9	121.0	52.6		
12	8.5	~ 0		
15	2.9	~ 0		

functionals, we found it impractical to use these for larger cells ($N \geq 9$).

The computational details are essentially identical to those presented in Sec. II except that the supercell is constructed with a lattice parameter of 2.504 Å, which is the computed equilibrium value for the PBE XC functional. Hybrid DFT calculations are performed as an additional single-point calculation starting from the converged PBE wave functions.³²

Table II displays the Néel temperatures for the AFM ground states obtained using different XC functionals. As seen, there is a systematic decrease in the Néel temperature going from LSDA to PBE to the two hybrid functionals. Interestingly, for the $N = 6$ case, the total magnetic moment for PBE, HSE06, and PBE0 XC functionals is 4 μ_B , as compared to 1.4 μ_B for LSDA. Thus, both the energetics as well as the magnetic properties are somewhat sensitive to the XC functional. Nevertheless, the key points made before still hold, namely, (a) C islands with zigzag edges embedded in an hBN matrix will display intrinsic magnetic moments and (b) the islands will preferentially couple antiferromagnetically to each other, the strength of the interaction being inversely proportional to their spacing.

¹S. J. Blundell and F. L. Pratt, *J. Phys. Condens. Matter* **16**, R771 (2004); M. N. Leuenberger and D. Loss, *Nature (London)* **410**, 789 (2001).

²T. Makarova, *Semiconductors* **38**, 615 (2004).

³W. L. Wang, S. Meng, and E. Kaxiras, *Nano Lett.* **8**, 241 (2008); O. Hod, V. Barone, and G. E. Scuseria, *Phys. Rev. B* **77**, 035411 (2008).

⁴Y.-W. Son, M. Cohen, and S. G. Louie, *Nature (London)* **444**, 347 (2006); O. Hod, V. Barone, J. E. Peralta, and G. E. Scuseria, *Nano Lett.* **7**, 2295 (2007); O. V. Yazyev and M. I. Katsnelson, *Phys. Rev. Lett.* **100**, 047209 (2008); A. Ramasubramaniam, *Phys. Rev. B* **81**, 245413 (2010).

⁵M. A. H. Vozmediano, M. P. Lopez-Sancho, T. Stauber, and F. Guinea, *Phys. Rev. B* **72**, 155121 (2005); O. V. Yazyev and L. Helm, *ibid.* **75**, 125408 (2007); P. O. Lehtinen, A. S. Foster, Y. Ma, A. V. Krasheninnikov, and R. M. Nieminen, *Phys. Rev. Lett.* **93**, 187202 (2004).

⁶T. G. Pedersen, C. Flindt, J. Pedersen, N. A. Mortensen, A.-P. Jauho, and K. Pedersen, *Phys. Rev. Lett.* **100**, 136804 (2008).

⁷A. Ramasubramaniam, N. V. Medhekar, and V. B. Shenoy, *Nanotechnology* **20**, 275705 (2009).

⁸D. W. Boukhvalov, M. I. Katsnelson, and A. I. Lichtenstein, *Phys. Rev. B* **77**, 035427 (2008); P. O. Lehtinen, A. S. Foster, A. Ayuela, A. Krasheninnikov, K. Nordlund, and R. M. Nieminen, *Phys. Rev. Lett.* **91**, 017202 (2003); M. Wu, E.-Z. Liu, and J. Z. Jiang, *Appl. Phys. Lett.* **93**, 082504 (2008).

⁹K. T. Chan, J. B. Neaton, and M. L. Cohen, *Phys. Rev. B* **77**, 235430 (2008).

¹⁰L. Brey, H. A. Fertig, and S. Das Sarma, *Phys. Rev. Lett.* **99**, 116802 (2007); M. Wu, C. Cao, and J. Z. Jiang, *Nanotechnology* **21**, 505202 (2010).

¹¹C. R. Dean, A. F. Young, I. Meric, C. Lee, L. Wang, S. Sorgenfrei, K. Watanabe, T. Taniguchi, P. Kim, K. L. Shepard, and J. Hone, *Nature Nanotechnology* **5**, 699 (2010).

¹²L. Ci, L. Song, C. Jin, D. Jariwala, D. Wu, Y. Li, A. Srivastava, Z. F. Wang, K. Storr, L. Balicas, F. Liu, and P. M. Ajayan, *Nature Mater.* **9**, 430 (2010).

¹³S. Enouz, O. Stéphan, J.-L. Cochon, C. Colliex, and A. Loiseau, *Nano Lett.* **7**, 1856 (2007); P. Ayala, R. Arenal, and A. Loiseau, *Rev. Mod. Phys.* **82**, 1843 (2010).

¹⁴R. Q. Wu, L. Liu, G. W. Peng, and Y. P. Feng, *Appl. Phys. Lett.* **86**, 122510 (2005); M. U. Kahaly and U. Waghmare, *J. Phys. Chem. C* **112**, 3464 (2008).

- ¹⁵R.-F. Liu and C. Cheng, *Phys. Rev. B* **76**, 014405 (2007).
- ¹⁶E.-J. Kan, X. Wu, Z. Li, X. C. Zeng, J. Yang, and J. G. Hou, *J. Chem. Phys.* **129**, 084712 (2008); S. Dutta, A. K. Manna, and S. K. Pati, *Phys. Rev. Lett.* **102**, 096601 (2009); Y. Ding, Y. Wang, and J. Ni, *Appl. Phys. Lett.* **95**, 123105 (2009); J. M. Pruneda, *Phys. Rev. B* **81**, 161409(R) (2010).
- ¹⁷B. Huang, C. Si, H. Lee, L. Zhao, J. Wu, B.-L. Gu, and W. Duan, *Appl. Phys. Lett.* **97**, 043115 (2010).
- ¹⁸J. Li and V. B. Shenoy, *Appl. Phys. Lett.* **98**, 013105 (2011); J. da Rocha Martins and H. Chacham, *ACS Nano* **5**, 385 (2011).
- ¹⁹N. Alem, R. Erni, C. Kisielowski, M. D. Rossell, W. Gannett, and A. Zettl, *Phys. Rev. B* **80**, 155425 (2009); J. C. Meyer, A. Chuvilin, G. Algara-Siller, J. Biskupek, and U. Kaiser, *Nano Lett.* **9**, 2683 (2009); C. Jin, F. Lin, K. Suenaga, and S. Iijima, *Phys. Rev. Lett.* **102**, 195505 (2009).
- ²⁰G. Kresse and J. Furthmüller, *Comput. Mater. Sci.* **6**, 15 (1996); *Phys. Rev. B* **54**, 11169 (1996).
- ²¹P. E. Blochl, *Phys. Rev. B* **50**, 17953 (1994); G. Kresse and D. Joubert, *ibid.* **59**, 1758 (1999).
- ²²J. P. Perdew and A. Zunger, *Phys. Rev. B* **23**, 5048 (1981).
- ²³D. M. Ceperley and B. J. Alder, *Phys. Rev. Lett.* **45**, 566 (1980).
- ²⁴E. H. Lieb, *Phys. Rev. Lett.* **62**, 1201 (1989).
- ²⁵The $N = 6$ case is further complicated by the average magnetic moment of each island itself being dependent upon the coupling to its neighbors (FM: $0.7\mu_B$, AFM: $\pm 1.19\mu_B$, as noted before).
- ²⁶R. J. Baxter, *Exactly Solved Models in Statistical Mechanics* (Academic Press, London, 1982).
- ²⁷A. L. Ivanovskii, *Phys. Usp.* **50**, 1031 (2007).
- ²⁸J. P. Perdew, K. Burke, and M. Ernzerhof, *Phys. Rev. Lett.* **77**, 3865 (1996).
- ²⁹J. Heyd, G. E. Scuseria, and M. Ernzerhof, *J. Chem. Phys.* **118**, 8207 (2003); **124**, 219906 (2006).
- ³⁰J. P. Perdew, M. Ernzerhof, and K. Burke, *J. Chem. Phys.* **105**, 9982 (1996); M. Ernzerhof and G. E. Scuseria, *ibid.* **110**, 5029 (1999).
- ³¹B. G. Janesko, T. M. Henderson, and G. E. Scuseria, *Phys. Chem. Chem. Phys.* **11**, 443 (2009).
- ³²VASP manual [<http://cms.mpi.univie.ac.at/vasp/vasp/>].